A Pt-Mo Hybrid Catalyst for Furfural Transformation.

Marta Stucchi [1,], Sharam Alijani[1], Maela Manzoli[2], Alberto Villa[1], Riikka Lahti [3], M.G. Galloni[1], Ulla Lassi [3] and Laura Prati[1].*

[1] Università degli Studi di Milano, Dipartimento di Chimica, Via Golgi 19, 20133, Milano, Italy.

[2] Dipartimento di Scienza e Tecnologia del Farmaco and NIS – Interdepartmental Centre for Nanostructured Interfaces and Surfaces, Università degli Studi di Torino, Torino, Italy.

[3] University of Oulu, Research Unit of Sustainable Chemistry, P.O. Box 4300, FIN-90014 Oulu, Finland.

Abstract

Furfural is a high-value chemical, being the precursor of compounds such as furfuryl alcohol and tetrahydrofurfuryl alcohol. Pt is known as active for furfural hydrogenation, but the high price limits its exploitation and imposes the search for alternatives. Here we presented a Pt/Mo bimetallic system with enhanced catalytic activity for furfural hydrogenation. For comparison, monometallic Mo- and Pt-supported on activated carbon have been prepared by impregnation and sol-immobilization. The bimetallic Pt/Mo was prepared impregnating the Mo-AC catalyst with Pt, using Na_2PtCl_4 as a precursor, PVA, and $NaBH_4$ as reducing agent. HR-TEM analyses on Pt/Mo catalyst showed Mo-containing agglomerates embedded in the carbon matrix, displaying diffraction fringes with spacing typical of Mo_4O_{11} in the orthorhombic phase, as well as Pt nanoparticles more evenly dispersed in the Mo-AC system compared to bare AC. The Pt/Mo catalyst showed higher activity than both monometallic ones, and it converted 92 % of furfural to furfuryl alcohol and ethyl furfuryl ether with 20 % and 80 % selectivity, respectively. However, despite a lower initial activity, the monometallic Mo/AC catalyst showed a complete selectivity to the ether.

Keywords:

Biomass valorization; Molybdenum-based catalysts; Furfural hydrogenation; Pt/Mo bimetallic structures; Mo_4O_{11} orthorhombic phase; Ethyl furfuryl ether.

1. Introduction

Biomass is a valid carbon-based alternative source for the production of renewable chemicals and fuels [1]. First-generation biomass consists of triglycerides, the main component of vegetable oils and oil-processing waste [2], while second-generation biomass consists of lignocellulose, which refers to the whole plant dry matter. It is the most abundantly available raw material and it is composed of carbohydrate polymers (cellulose, hemicellulose) and an aromatic polymer (lignin). Xylose is the major product of hemicellulose hydrolysis [3], from which furfural is easily obtained by acid catalysis [4, 5]. Furfural has been identified as a very interesting compound, considering the possibility to directly obtain valuable chemicals, such as furfuryl alcohol (FFA) and tetrahydrofurfuryl alcohol (THFA) from its hydrogenation [6, 7]. Heterogeneous catalysis efficiently converts biomass. The easier catalysts recovery and their higher durability make it more advantageous than homogenous or enzymatic systems [8]. Noble metal-based catalysts were the most exploited for biomass transformation [9], due to their valid activity and stability under acidic, basic and aqueous conditions [10]. Pd, Ru and Pt were the most exploited metals for catalytic reactions [11; 12; 13; 14]. Platinum has been known as a furfural hydrogenation catalyst [15]. Mikolajska et al. [16] firstly investigated Pt deposited on monolayer supports for the selective hydrogenation of furfural. Pt/SiO_2 showed the highest catalytic performance by converting 68 % of substrate, followed by Pt/TiO_2 (yield= 33.5 %, selectivity= 61.2 %). However, the main reaction product was 2-methylfuran formed by hydrogenolysis. After, Mahajani et al. [17] reported the kinetics of the liquid-phase hydrogenation of furfuraldehyde to furfuryl alcohol over a 5% Pt/C catalyst, proving their efficiency and reusability. Another more recent paper reported that Pt nanoparticles on MgO, CeO_2, or γ-Al_2O_3 catalyze selectively furfural hydrogenation. The role of the solvent is also investigated, showing that methanol or n-butanol promoted high furfural alcohol yields, contrariwise to non-polar solvents that led to poor furfural conversion [18]. Furfural selective hydrogenation can be obtained by Pt nanoparticles, and tuned through controlling the support, reaction solvent or temperature; however, one of the major issues related to the use of Pt is the high market price. Many researches demonstrated that the catalytic properties of some cheaper metal carbide are comparable to the catalytic properties of the more expensive Pt-groups metals. For example, Villa et al. [19] tested Mo and W carbide in the liquid phase oxidation of benzyl alcohol proving their good activity and the tunability of the selectivity depending on the reaction medium. Patel et al. proposed a Mo_2C/Al_2O_3 catalyst to improve the catalytic pyrolysis of sugarcane, increasing the yields of furans and phenols [20]. Moreover, β-Mo_2C/Al_2O_3 efficiently catalyzed the sunflower oil hydro-treatment for the production of biofuels [21]. A Mo-doped Co catalyst exhibited a very high activity and selectivity during the liquid phase hydrogenation of furfural (FF) [22], because Mo in the form of MoO_3 showed a promoting effect on the hydrogenation activity, favoring the adsorption of the furfural carbonyl group. In fact, many papers report the advantageous effects of bimetallic catalysts [23].

Bimetallic structures consisting of Mo and Pt already showed higher activity than monometallic ones in hydrogenolysis of alkanes [24] and dehydrogenation of cyclohexane [25]. Lee and Choi [26] also studied the specific structure of Mo-Pt supported on γ-alumina by XAFS, highlighting both a strong interaction of Mo atoms with the support, and proving that Pt influenced the electronic state of Mo. From these results, here we prepared and investigated the catalytic activity for furfural conversion of a new Mo-supported on activated carbon (AC), first. Mo/AC was compared with a Pt /AC as catalyst for the same reaction. Moreover, the Mo/AC has been modified with Pt.

2. Experimental

2.1 Support preparation method

Carbonization and activation of birch sawdust was performed in a single-step process using a rotating quartz reactor (Nabertherm GmbH RSRB 80). The carbonization step was performed under an N_2 flow (200 ml min^{-1}) at 800 °C (heating ramp of 6.7 °C min^{-1}). During the activation the temperature was kept at 800 °C for 120 minutes with a stream of water steam and N_2 gas (120 g h^{-1} at 140 °C and 200 ml min^{-1}, respectively). The resulting activated carbon was crushed and sieved to a fraction size of < 50 μm [27; 28].

2.2 Synthesis of Mo-supported catalysts

Mo-supported AC was prepared by incipient-wetness impregnation method. The metal precursor was $(NH_4)_6Mo_7O_{24} \cdot 4H_2O$, calculated in order to obtain a loading of 40 wt.% and 10 wt.% Mo, respectively. The precursor was dissolved in a water amount such as the calculated pore volume (0.26 ml g^{-1}) and mixed with the suitable amount of AC. The mixture was placed in a Rotavapor at room temperature for 16 h (20 rpm). The material was then dried overnight in an oven at 105 °C and then calcined in a CVD oven at 350 °C for 5 h with N_2 flow (250 ml h^{-1} per g of catalyst). Samples were labelled as 10- and 40%Mo@AC, respectively (Table 1).

2.3 Synthesis of mono- and bimetallic Pt-Mo supported catalysts

We synthesized a 1 % Pt-supported catalyst by sol-immobilization [29], using activated carbon from birch [28] as support. Activated carbon deriving from birch sawdust was prepared by carbonization and activation, in a single-step process at 800 °C, as reported in detail elsewhere [28]. The ash content is 8.5 %, while C and O % from elemental analysis are 92.4 % and 2.1 %, respectively. A

Na_2PtCl_4 solution ([metal] = 10 mg ml^{-1}) was the precursor. 1 ml of the precursor was dissolved in 100 ml of water (milli-Q), and PVA (Pt/PVA ratio = 1:0.5) (Polyvinyl alcohol, MW=9,000–10,000, 80% hydrolyzed, Aldrich) was added under stirring. After 5 min $NaBH_4$ ($NaBH_4$: Pt 4:1 mol/mol) was added and stirring continued for 4 hours at room temperature (RT). Finally, we added the carbon support. The sample was filtered, washed and later dried at 80 °C. By the same procedure, finally we impregnated Pt nanoparticles on 40%Mo@AC sample. The samples were labeled as reported in Table 1.

Table 1. Samples list.

#	Sample name	Support	Precursor
1	10%Mo@AC_birch	AC_birch	$(NH_4)_6Mo_7O_{24} \cdot 4H_2O$
2	40%Mo@AC_birch	AC_birch	$(NH_4)_6Mo_7O_{24} \cdot 4H_2O$
3	1%Pt@AC_birch	AC_birch	Na_2PtCl_4
4	1%Pt/Mo@AC_birch	40%Mo@AC_birch	Na_2PtCl_4

2.4 Characterization

The metal content of Mo-doped samples was measured by ICP-OES using a Perkin Elmer Optima 5300 DV instrument. Samples were mixed with HCl (37 %) and HNO_3 (63 %) and digested in a microwave oven (MARS, CEM Corporation) at 200 °C for 10 min. The Pt content was confirmed by ICP on the exhausted impregnation solution.

Specific surface area and porosity distribution were obtained from N_2 adsorption/desorption isotherms at 77 K using a Micromeritics Tristar II 3020 apparatus and applying Brunauer–Emmett–Teller (BET) and Barrett–Joyner–Halenda analyses, respectively [30]. Prior to measuring, sample powders were heat-treated (T = 150 °C, 4 h, N_2) to remove adsorbed foreign species.

Thermo Fisher Scientific ESCALAB 250Xi XPS System performed X-ray photoelectron spectroscopy analysis (XPS). We analyzed data by Avantage V5. The monochromatic AlKα radiation (1486.7 eV) operated at 20 mA and 15 kV. Charge compensation was used to determine the presented spectra, and the calibration of the binding energies (BE) was performed by applying the C1s line at 284.8 eV as a reference.

A PANalytical X´Pert Pro X-ray diffraction equipment, using monochromatic CuKα1 radiation (λ=1.5406 Å) at 45 kV and 40 mA recorded the X-ray diffractograms (2θ range of 5-80° at 0.017° intervals and with a scan step time of 110 s). The crystalline phases and structures were analyzed by HighScore Plus program. Particles morphology of Mo-based catalysts was studied by a energy filtered

transmission electron microscope (EFTEM, instrument resolution 0.37 nm) LEO 912 OMEGA, using an accelerating voltage of 120 kV and an emission current of 8-15 μA, respectively.

Further transmission electron microscopy (TEM) and high resolution (HR-)TEM characterization of the 40%Mo@AC, 1%Pt@AC and 1%Pt/Mo@AC catalysts was performed by using a side entry JEOL 3010-UHR HRTEM microscope operating at 300 kV, equipped with a LaB_6 filament, with a (2*k*×2*k*)-pixel Gatan US1000 CCD camera and with an OXFORD INCA EDS instrument for atomic recognition via energy dispersive spectroscopy (EDS). The powdered samples were deposited on copper grids, coated with a porous carbon film. A statistical evaluation of the size of the Pt particles was performed and histograms of the particle size distribution were obtained by considering at least 150 particles on the images. The mean particle diameter (d_m) was calculated as:

$$d_m = \Sigma d_i n_i / \Sigma n_i$$

where n_i was the number of particles of diameter d_i. The counting was carried out on electron micrographs acquired starting from 100,000 magnifications, where Pt nanoparticles contrasted with respect to the AC and 40%Mo@AC supports were detected. To investigate the molybdenum phase, the Fourier Transformed (FT) of a representative number of images collected for 40%Mo@AC and 1%Pt/Mo@AC were analysed.

2.5 Catalytic reaction

10% and 40%Mo-AC have been firstly compared in furfural hydrogenation at 150 °C and 3 bar of H_2. Reaction was performed in a batch homemade autoclave (75 ml volume), having a substrate/metal ratio of 10 g/g in 10 ml of furfural solution 0.3 M in EtOH. Considering the reaction conditions usually set for Pt-based catalysts, the further reactions to compare Pt/AC, Mo/AC and the Pt/Mo system were performed at 50 °C and 3 bar of hydrogen, with substrate/metal ratio of 500 (mol/mol). GC analyses showed the furfural conversion and products formation over time (6 h), given by a GC-MS (Thermo Scientific ISQ QD equipped with an Agilent VF-5ms column). The internal standard was dodecanol. We compared resulting fragmentation peaks with standards present in the software database, while a GC-FID equipped with a non-polar column was employed (Agilent 7820A equipped with an Agilent CP-Sil 5 CB column) to quantify the amounts of reactants consumed and products generated. Furfural conversion was calculated as mol converted divided per the starting mol of the substrate, considering the starting concentration (0.3 M) and the reaction volume (10 ml). Selectivity has been calculated at maximum conversion, considering that all the reaction of furfural hydrogenation did not reach complete substrate conversion.

3. Results and discussion

3.1 Characterizations

3.1.1 Textural and surface properties

AC from birch sawdust showed a SSA of 883 m^2 g^{-1} (Table 2).

Table 2. Characterization of activated carbon supports and Mo-supported samples.

	BET (m^2 g^{-1})	Pore volume (cm^3 g^{-1})	Me % (ICP)
AC-Birch	*883*	*0.66*	-
10%Mo@AC	500	0.40	9.0
40%Mo@AC	283	0.26	38.1
1%Pt@AC	735	0.13	1.0
1%Pt/40%Mo@AC	243	0.03	1.0

The deposition of metal species reduced the SSA. The decrease of SSA was proportional to the metal loading (Table 2). ICP analyses showed the exact metal content. The lowest Mo loading resulted in a more homogeneous dispersion of the particles, according to Figure 2 XRD analyses (Fig. 1A) showed mostly the presence of Mo^{+6} (JCPDS file number 00-065-0141) for 10%Mo@AC, while 40%Mo@AC (Fig. 1B) showed the presence of the orthorhombic Mo_4O_{11} phases (JCPDS file number 00-005-0337).

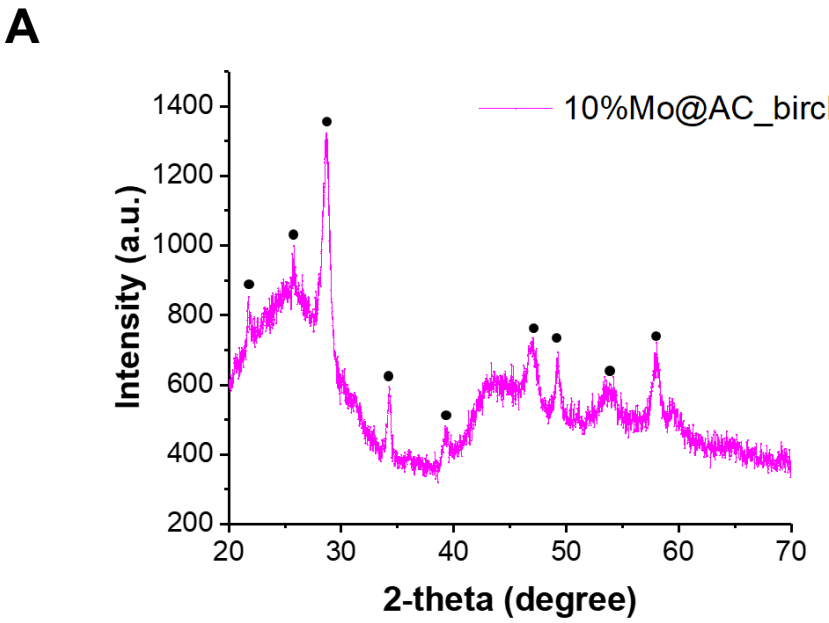

B

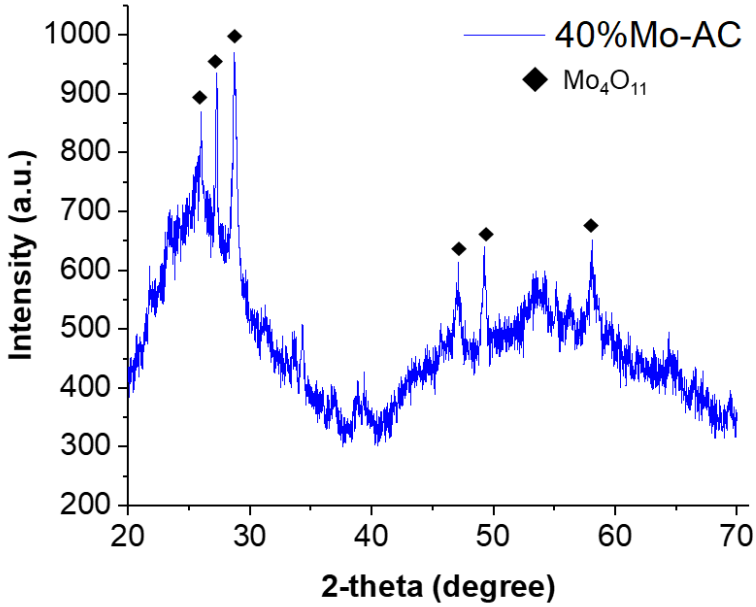

Figure 1. XRD spectra of 10%Mo@AC_birch (A) and 40%Mo@AC_birch (B).

3.1.2 XPS analyses

Table 3. XPS analysis of 40%Mo@aAC, 1%Pt@AC and 1%Pt/40%Mo@AC.

Catalyst	**O1s**				**C1s**				**Mo3d** $_{5/2}$		**Pt4f** $_{7/2}$		
	C=O	C-O-C	C-O-H	O-C=O	C-C C-H	C-O	C=O	O-C=O	Mo (IV)	Mo (VI)	Pt^0	Pt^{+2}	Pt^{+4}
40%Mo@AC													
BE (eV)	530.2	531.7	533.5	-	284.6	286.0	287.5	-	230.8	232.2	-	-	-
Rel. am. %	26.0	46.0	28.0	-	60.5	31.4	8.1	-	67.6	32.4	-	-	-
1%Pt@AC													
BE (eV)	530.9	532.4	533.6	534.9	284.6	285.6	287.2	-	-	-	71.2	72.1	74.9
Rel. am. %	10.6	53.3	23.7	12.4	58.5	34.6	6.9	-	-	-	6.3	52.0	41.6
1%Pt/40%Mo@AC													
BE (eV)	531.4	532.4	533.4	534.8	284.6	286.0	-	288.5	231.0	232.6	71.7	72.7	74.3
Rel. am. %	50.7	19.1	25.8	4.4	48.1	47.1	-	4.7	97.4	2.6	36.7	27.1	36.2

X-ray photoelectron spectroscopy (XPS) of the different metal-impregnated samples was performed to investigate the surface chemistry of the carbon support and the oxidation state of the metal species. We collected the survey spectra (Fig. S1 A-C, supporting information) and the high-resolution spectra for each sample (Fig. S2, S3 and S4, supporting information). The chemical species present on the surface and their relative amount are summarized in Table 3. Monometallic catalyst showed a higher graphitization degree compared to the 1%Pt/40%Mo@AC. The oxygen chemistry is dominated by the presence of C-O groups as indicated by the signal at binding energy (BE) 285.6-286.0 eV for C1s species. However, the contribution at BE 287.2-287.5 eV evidenced the presence of C=O groups only for monometallic samples; for 1%Pt/40%Mo@AC, the signal at BE 288.5 eV evidenced the presence of the carboxyl functionalization. Considering the O1s species, only the Pt-modified samples showed the signal at BE 534.8-534.9 eV that indicated the presence of O-C=O groups. Moreover, the signal at BE 530.2-531.4 eV, which refers to the C=O groups, is definitely larger for 1%Pt/40%Mo@AC, contrarily to both Pt- and Mo-AC where the largest contribution comes from the signal at BE 531.7-532.4 eV, indicating a chemistry dominated by the presence of C-O-C groups. The high-resolution spectra showed the presence the oxidation states of Mo(IV) and Mo(VI) (Fig. S4, supporting information), and the presence of metal Pt, PtO, and PtO_2 (Fig. S4, supporting information), for Mo- and Pt-based catalyst, respectively. It is very interesting to see that, in the bimetallic Pt-Mo system, the distribution of the various oxidized species was different. In particular, the relative amount % of Mo(IV) is higher in the case of 1%Pt/40%Mo@AC, where it represents almost all the metal oxidation state. Also the distribution of the Pt oxidation states is different in the Pt-Mo bimetallic system, where the larger signal at BE 71.7 eV evidenced an higher presence of Pt in metal form.

3.1.3 TEM analyses

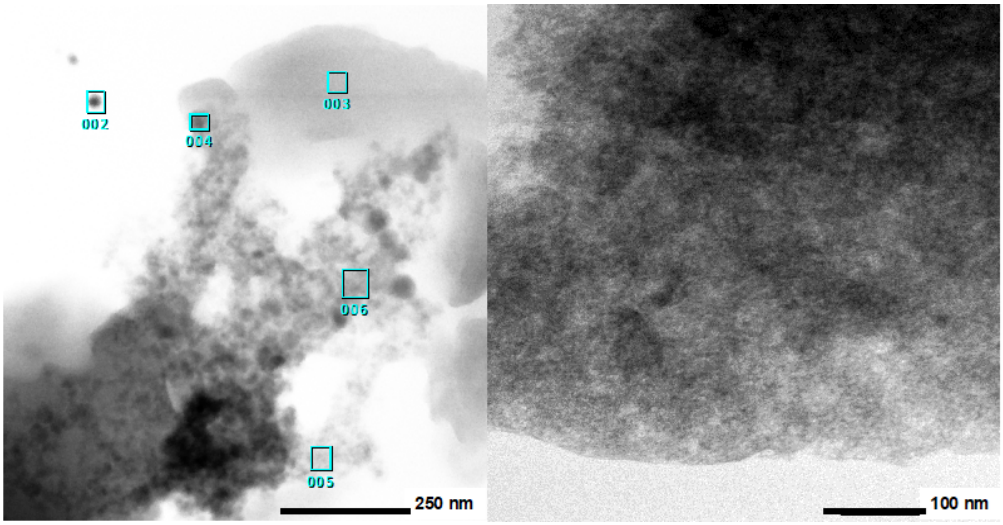

Figure 2. Representative TEM images of 10%Mo@AC at different magnifications.

The results of TEM and HR-TEM characterization performed on the 40%Mo@AC sample are shown in Figure 3. Big and well contrasted Mo-containing agglomerates, whose composition was confirmed by EDS analysis (Figure 4), embedded in a carbon matrix were observed (section a of Figure 3).

At higher magnification, such needle-shaped crystals display diffraction fringes with spacing (according to the corresponding FT and spacing in c and d, respectively) typical of Mo_4O_{11} in the orthorhombic phase (JCPDS file number 00-005-0337), in agreement with XRD.

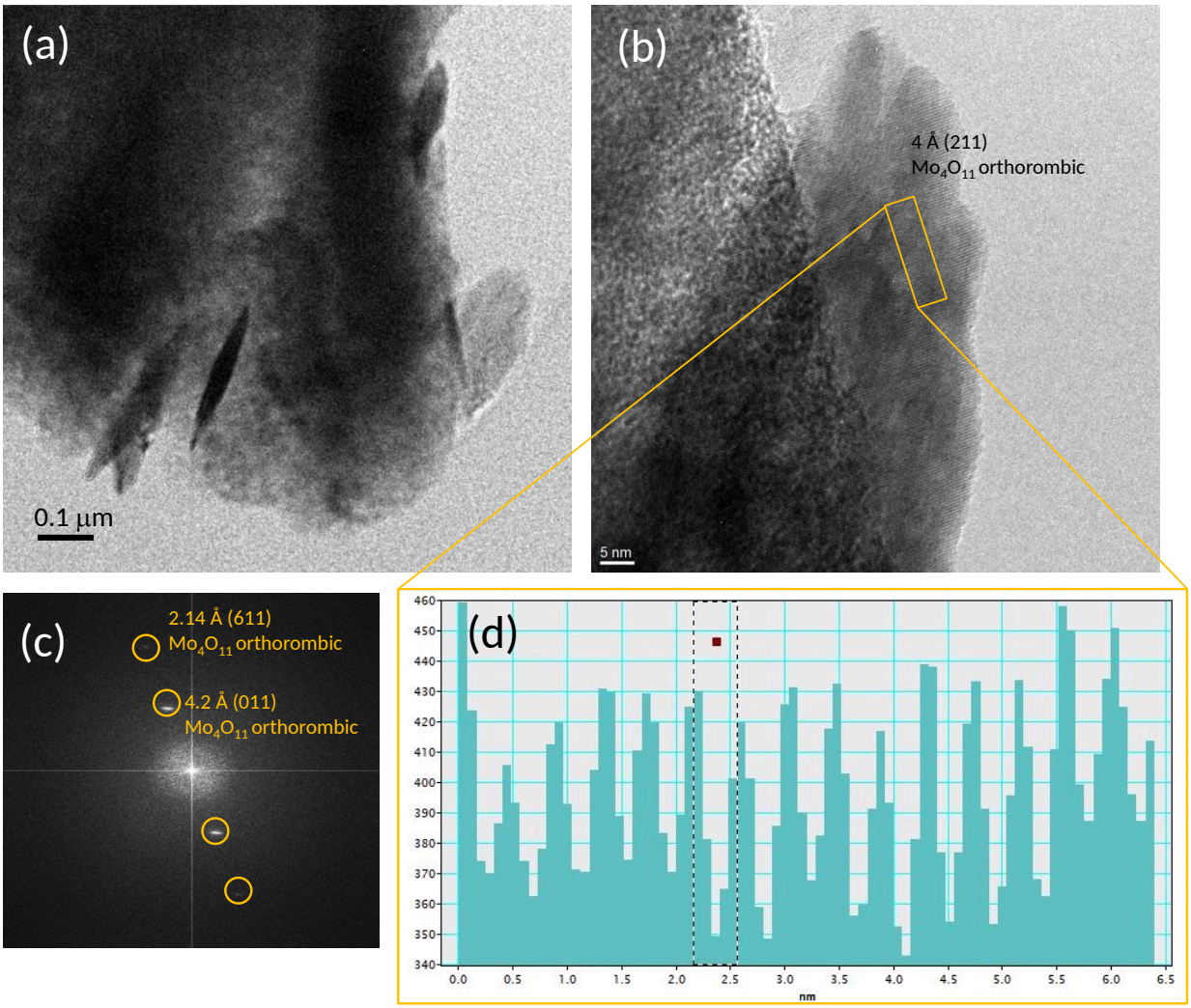

Figure 3. Representative TEM (a) and HR-TEM (b) images of 40%Mo@AC. (c) FT of the HR-TEM image reported in (b). (d) evaluation of the distance among the diffraction fringes observed in (b). Instrumental magnification: 20000X and 250000X, respectively.

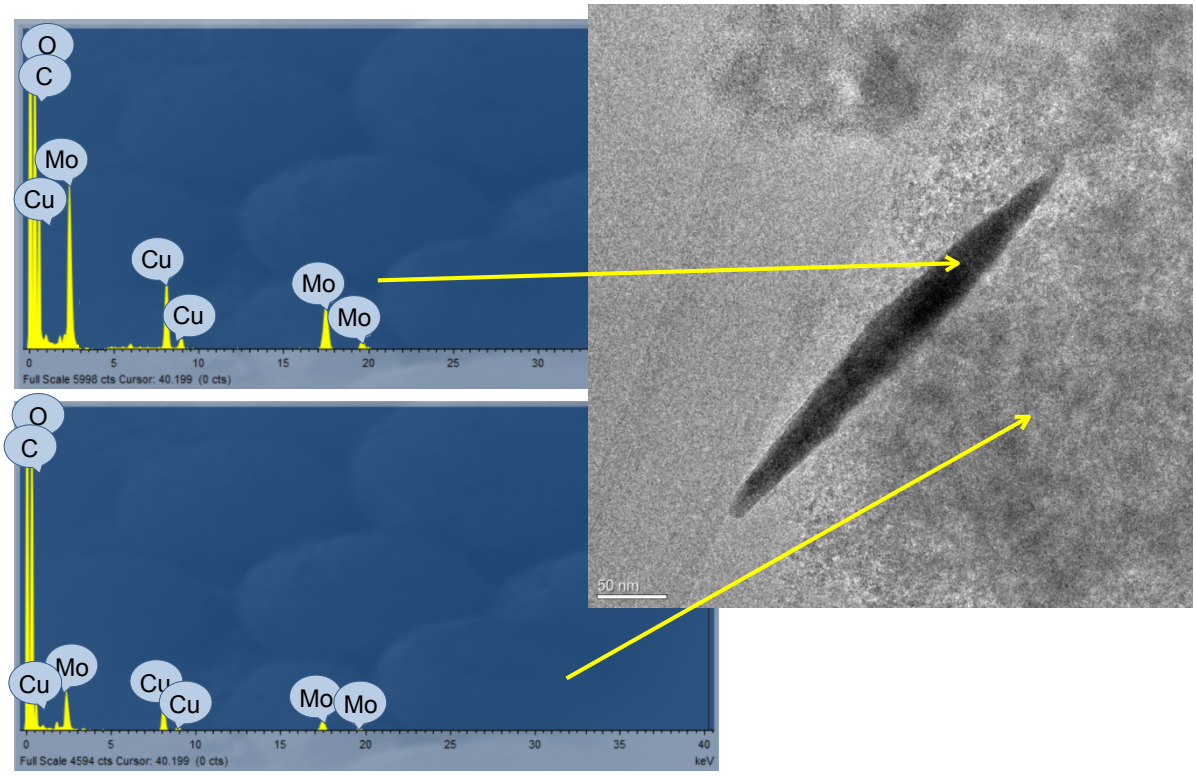

Figure 4. Representative TEM image of 40%Mo@AC and EDS spectra of a Mo-containing crystal and a carbon-rich region. Instrumental magnification: 50000X.

TEM and HR-TEM measurements have been also performed on 1%Pt@AC (Fig. 5) and 1%Pt/Mo@AC (Fig. 6) catalysts. Highly contrasted Pt nanoparticles with particle size of 3.5 ± 0.8 nm (Figure 5, section b) were easily recognizable on the AC support as can be appreciated in sections a and c, where some representative images taken on 1%Pt@AC are reported.

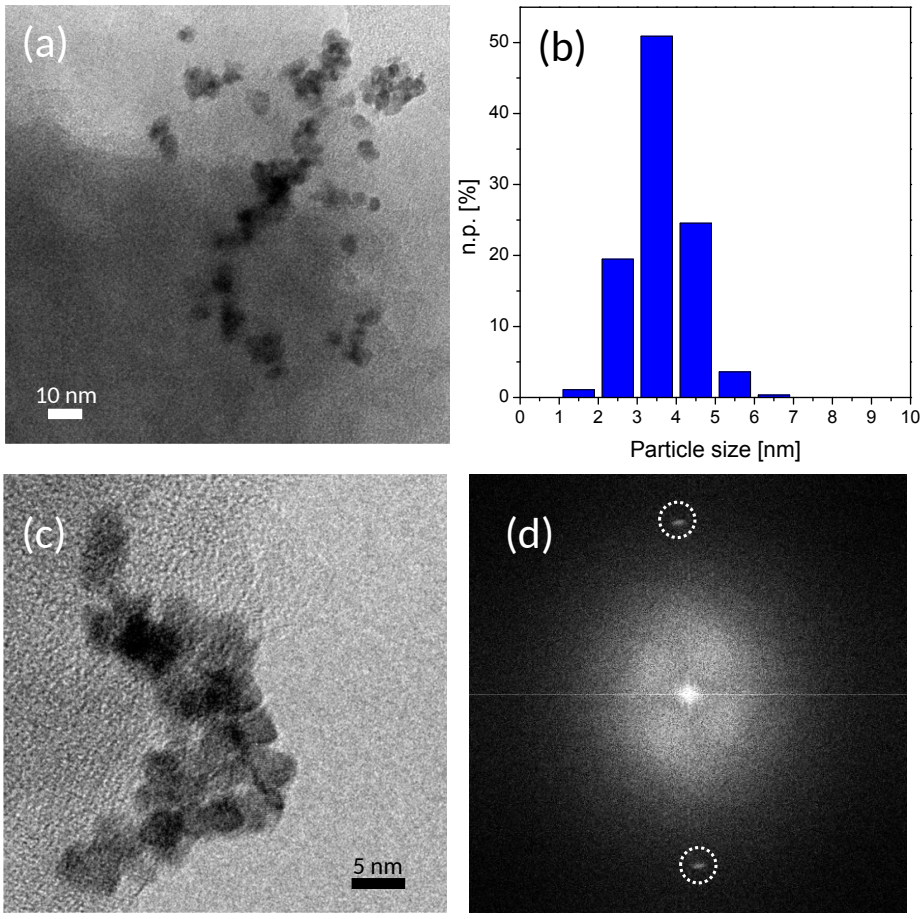

Figure 5. Representative TEM (a) and HR-TEM (c) images and Pt particle size distribution (b) of 1%Pt@AC. (d): FT of the HRTEM image reported in (c). Instrumental magnification: 100000X and 250000X, respectively.

In addition, the points in the FT, that are highlighted by dashed circles in section (d), as well as the lattice fringes in the image (section c) put in evidence a distance between the planes of 1.96 Å that can be attributed to the (200) plane of Pt in the cubic phase (JCPDS file number: 00-001-1190). Moreover, despite the quite high dispersion obtained, it was observed that these crystalline nanoparticles tend to form small agglomerates, thus lowering the metal exposed surface area.

Analogously to what observed for the 40%Mo@AC sample, the presence of big Mo-containing aggregates, well contrasted with respect to the AC was found also in the case of the 1%Pt/Mo@AC catalysts, as shown in Figure 6, section a. In addition, highly dispersed Pt nanoparticles, highlighted by white arrows in sections b and c, were observed by HR-TEM analyses.

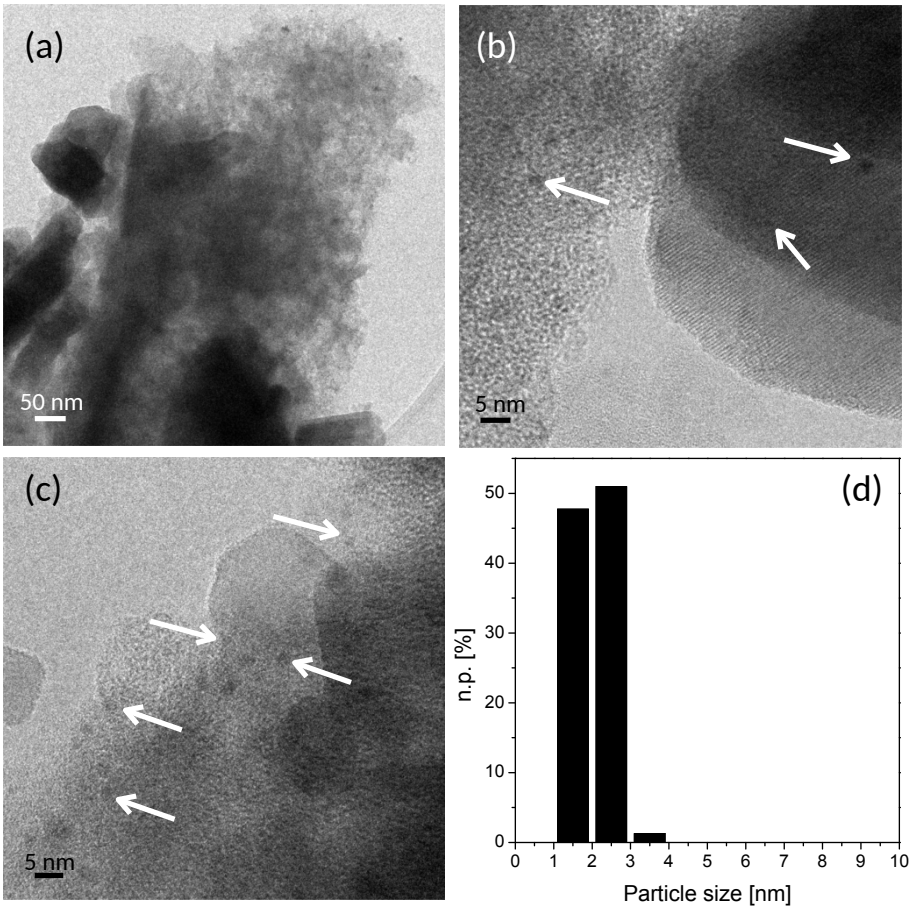

Figure 6. Representative TEM (a) and HR-TEM (b, c) images and Pt particle size distribution (d) of 1%Pt/Mo@AC. Instrumental magnification: 30000X, 250000X and 250000X.

The characterization put in evidence that such nanoparticles are homogeneously distributed on the 40%Mo@AC support, either on the AC region or on the Mo-rich region and have mean diameter d_m= 1.8 ± 0.4 nm (Figure 6, section d).

To further investigate the distribution of the Pt nanoparticles within the catalyst, additional TEM measurements combined with EDS analysis have been carried out and the results are shown in Figure 7.

In particular, the relative spatial distribution of the different elements, such as Pt (b, red map), Mo (c, blue map), O (d, orange map) and C (e, white map) within the 1%Pt/Mo@AC catalyst has been measured by EDS mapping performed on the region of the 1%Pt/Mo@AC catalyst shown in section (a). According to the red map reported in section (b), an homogeneous distribution of Pt was observed confirming the uniform distribution of the metal nanoparticles. Moreover, the uniformity of the points in the Mo (c), O (d) and C (e) maps indicated that the Mo-containing phase and the AC support are close and interacting with each other and not separated in distinct zones of the catalyst.

Basing on these findings, an effect of the presence of the Mo_4O_{11} phases on the Pt dispersion can be inferred.

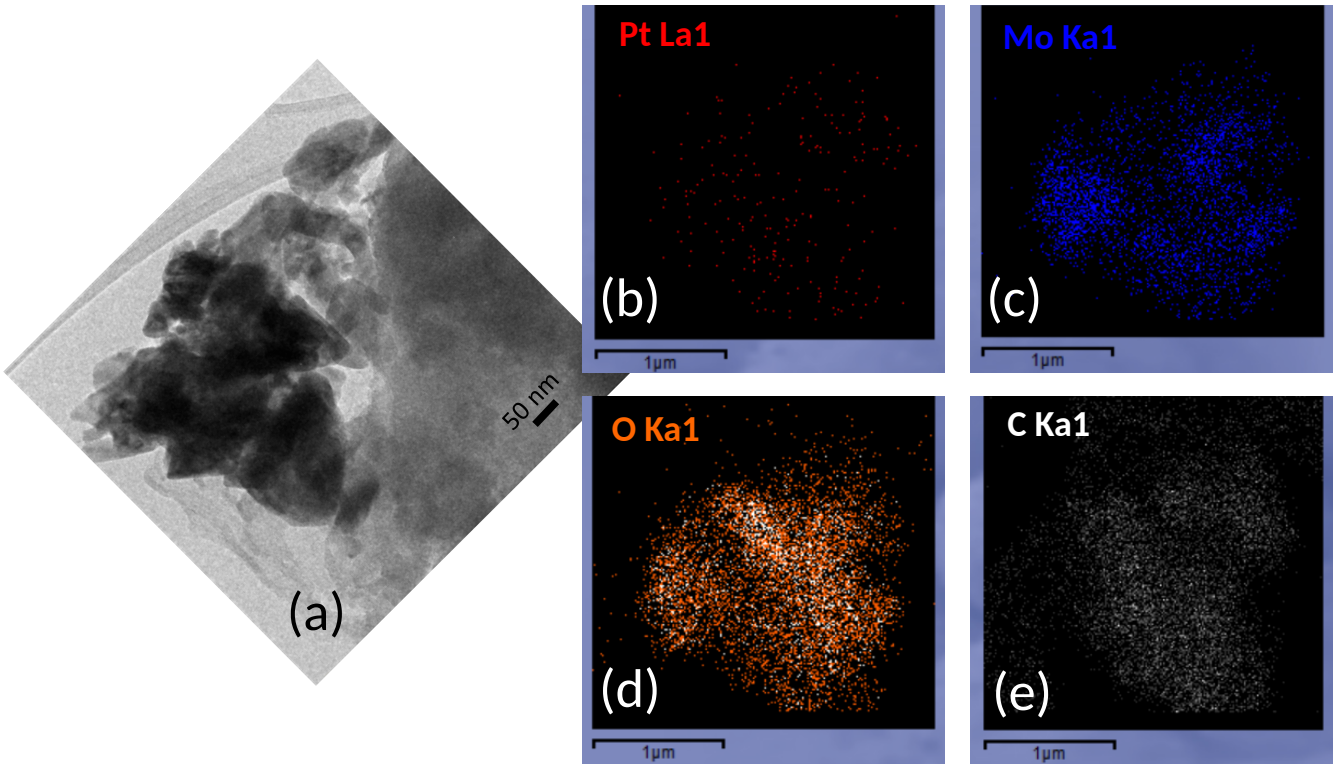

Figure 7. Selected TEM micrograph (a) representing sample 1%Pt/Mo@AC. EDS map of the same region showing the relative location of Pt (b), Mo (c), O (d) and C (e). Instrumental magnification: 30000X.

XRD analysis confirmed the presence of Pt and Mo_4O_{11} orthorhombic phase (Fig. 8). XRD peaks at 2-theta 23.6°, 25.9°, 27.5° and 46.5°, 49.5°, 59.1° degrees (black rhombus) can be attributed to Mo_4O_{11}, while a smaller fraction of Pt is confirmed by the peaks at 2-theta 39.2° and 64.9°.

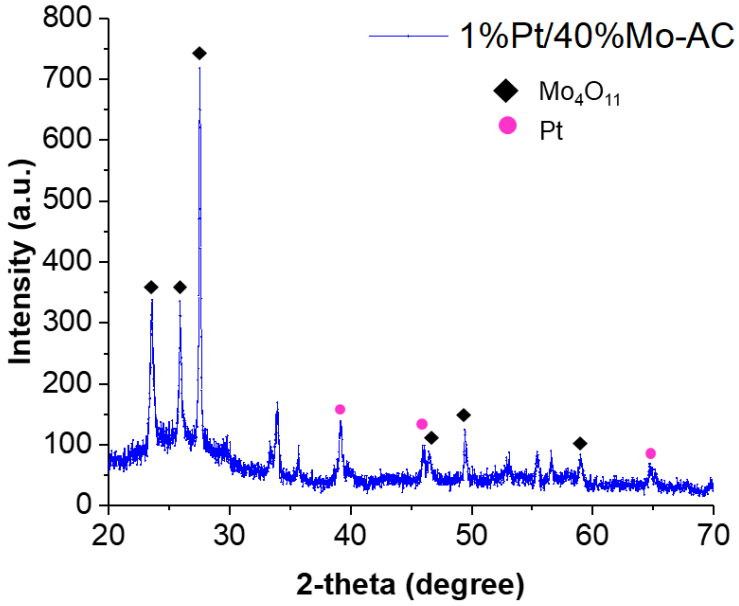

Figure 8. XRD pattern of the 1%Pt/40%Mo-AC. Pt peaks marked as (●); Mo_4O_{11} peaks marked as (♦).

3.2 Activity

All the catalysts have been tested in furfural hydrogenation in a batch autoclave. The first comparison between 10%- and 40%Mo-AC has been performed working at 150 °C and 3 bar of H_2 (Fig. 9). 40%Mo@AC reached 89 % conversion while 10%Mo@AC reached only 60 % conversion, with a reaction profile which reached a plateau after 6 h (reaction profile by square points, fig. 9). In this case the catalyst amount was fixed in order to have a substrate/metal ratio of 10 g/g. Both the catalysts converted furfural to ethyl furfuryl ether (FEE) with > 99 % selectivity. Here, FEE may derive from the reaction between FFA and the solvent, i.e. EtOH, as reported by C. Hammond et al. [31]. Wang et al. [32] also reported the synthesis of furfuryl ethyl ether (FEE) via the reductive etherification of furfural in ethanol at 60 °C on Pd/C catalysts. A more specific study of the reaction mechanism indicates that furfuryl ethyl ether is formed by protonation of furfuryl alcohol or furfuryl acetate followed by SN2-substitution of the leaving group by the nucleophilic ethanol [33]. Literature reports many publications about furfuryl ethers production, due to the fact that they are promising components of gasoline due to their high stability and high octane numbers [31]. In particular, the ethyl furfuryl ether can be produced in significant amount converting furfuryl alcohol in the presence of mild acidic catalysts such as zeolites [34]. Precisely, the production and uses of pure ethyl furfuryl ether as a fuel was patented by Shell [35], where in the presence of a powdered ZSM-5 catalyst and a 7.5:1 molar mixture of

EtOH/FFA, this latter was converted to EFE in a maximum yield of 50 mol% with 80% conversion and 62.5 % selectivity.

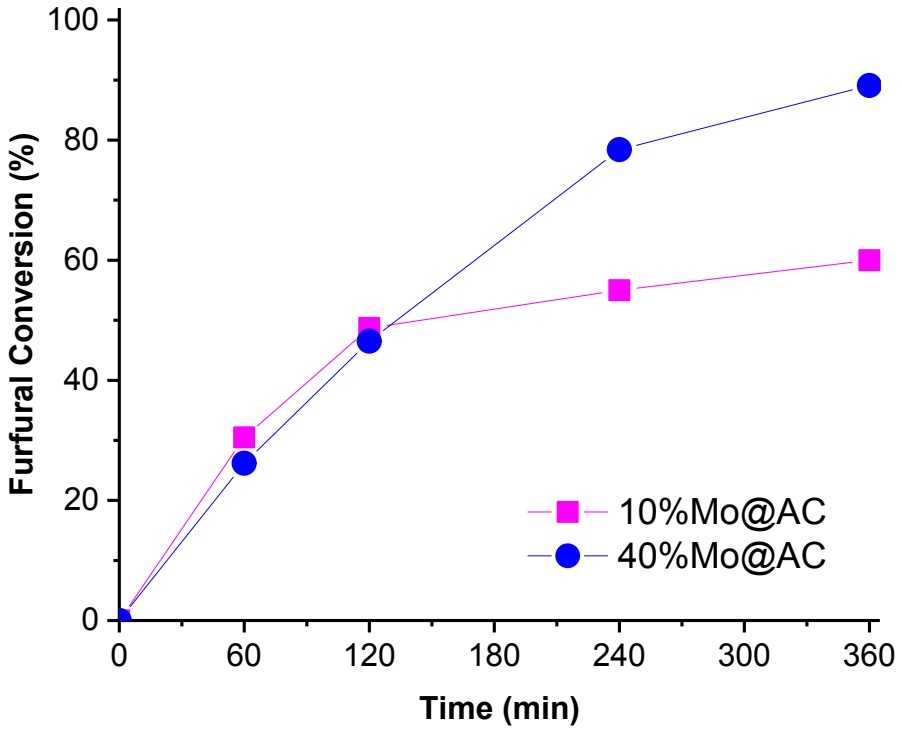

Figure 9. Furfural conversion % over time by Mo-based catalysts with different Mo loading. Hydrogenation conditions: 150 °C, p H_2 3 bar and substrate/metal ratio=10, g/g in 10 ml of furfural solution (0.3 M in EtOH).

The higher activity of the catalyst with higher Mo loading could have different explanations. In this regard, Chen et al. [36] studied the hydrogenation of furfural to furfuryl alcohol over Mo-doped catalysts, showing that catalytic activity depended on Mo amount, increasing proportionally until a certain value and then decreasing. In that case Mo favored the adsorption of C=O group of furfural due to its acidic properties; however, too high Mo amounts can be harmful due to the covering of surface active sites by Mo-oxides. Abello et al. [37] studied the oxidative dehydrogenation of propane over MoO_3/γ-Al_2O_3 catalysts with different Mo loading; increasing Mo loading decreased the SSA, while it increased the total acidity, generating new Brønsted acid sites. This latter is in agreement with the results of the acidity measurements (Table S1). Catalytic results showed also in this case a clear dependence on the molybdenum content, increasing the substrate conversion with Mo loading parallel

to the acidity and to the reducibility. Moreover, only the 40%Mo@AC showed the presence of Mo_4O_{11} orthorhombic phase, which can be another reason of its higher activity in furfural hydrogenation.

Depending on this preliminary results, we selected 40%Mo@AC for the further modification with Pt. We thus compared 40%Mo@AC, 1%Pt@AC 1%Pt/40%Mo@AC in furfural hydrogenation, working at 50 °C and 3 bar of H_2 accordingly to the standard conditions used with Pt-based catalysts (Fig. 10) [38].

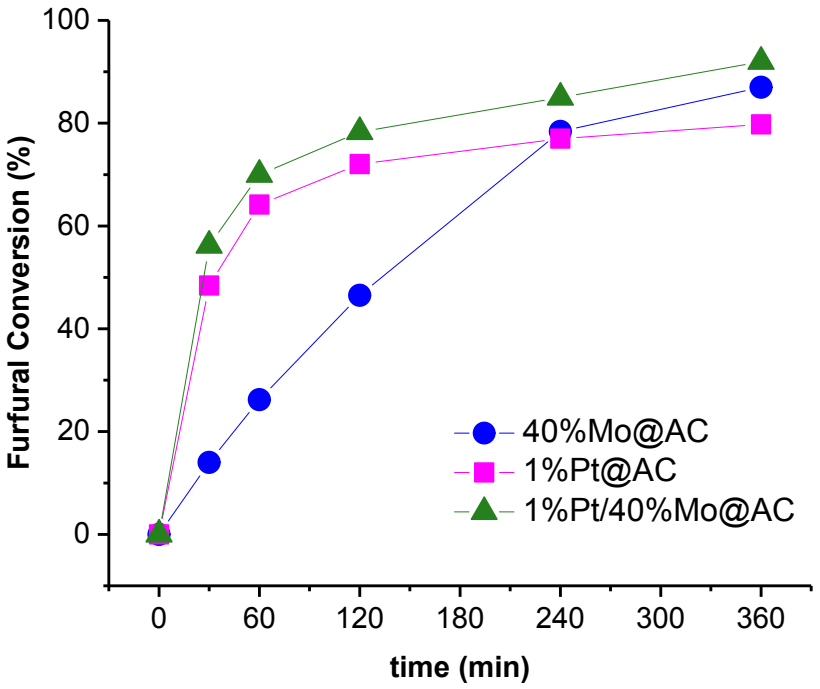

Figure 10. Furfural conversion % over time by Mo- (full rhombus), Pt- (full squares) and Pt-Mo (full dots) supported on AC, respectively. Hydrogenations occurred at 50 °C, 3 bar of H_2, Me/Substrate ratio of 1:500 in 10 ml of FF 0.3 M in EtOH.

Table 4. Furfural conversions by Pt/Mo catalysts and catalytic activities. Hydrogenations lasted 6 h at 50 °C and 3 bar H_2.

sample	conversion % [a]	Activity (h^{-1})[b]
40%Mo@AC	87.0	140
1%Pt@AC	79.7	484
1%Pt/40%Mo@AC	92.0	562

[a] conversion at 6 h
[b] Initial activity calculated after 30 min reaction, as [mol converted/mol metal*h]

The initial activity of both Pt@AC and Pt/Mo@AC was much higher than Mo@AC (Fig. 9 and Table 4). Moreover, they showed a different product distribution converting furfural to FEE with 80 % selectivity and FFA, with 20 % selectivity (Fig. 11). However, following the reaction profiles only Mo@AC did not show deactivation after 6 h of reaction (see circle points in fig. 10). Catalyst deactivation was marked in the case of Pt@AC, while it was less evident for Pt/Mo system. The synergistic effects of Pt and Mo_4O_{11} on the electrocatalytic activity displayed by a composite Magnéli phase Mo_4O_{11}, and Pt-black catalyst, were reported recently by Liu et al. [39]. The authors found strong metal-support interaction between the Pt and Mo_4O_{11} in addition to the various valence states of Mo (IV–VI) coexisting in Mo_4O_{11}, which may promote hydrogen spillover, result in the improvement of the poisoning tolerance and of the electrocatalytic activity of the catalyst. Thus, the presence of the Mo_4O_{11} orthorhombic phase (confirmed by TEM and XRD) could play a fundamental role in determining the high catalytic activity of Pt@Mo/AC. However, it could be also depended on the higher Pt nanoparticles dispersion and narrower particle size distribution.

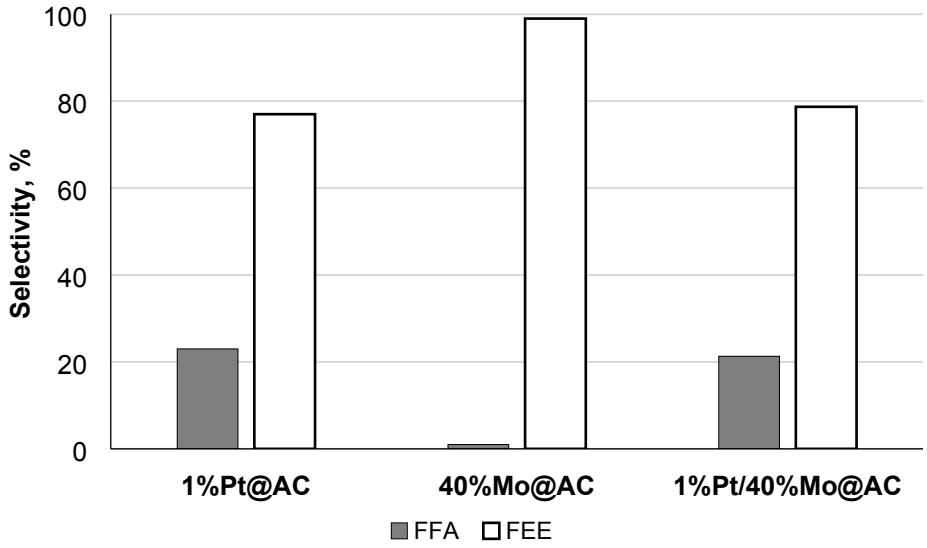

Figure 11. Main products selectivity from furfural hydrogenation by 1%Pt@AC, 40%Mo@AC and 1%Pt/40%Mo@AC, respectively.

3.3 Recycling tests

We also investigated the life-time of the bimetallic Pt-Mo system, as the most active catalyst. Recycling test were carried out by simply filtering the catalyst and re-using it without any further treatment. Each reaction lasted 60 min. Despite a slightly decrease in furfural conversion after the first two recycles, it stabilized and remained constant until the fifth test, proving a rather good stability of the catalyst (Fig. 12).

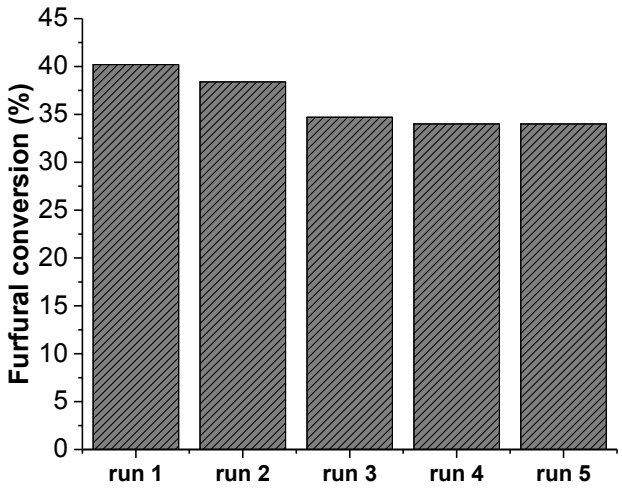

Figure 12. Reusability tests on 1%Pt/40%Mo-AC. Reaction conditions: Substrate concentration 0.3 M, Me:substrate molar ratio 1:500, 50 °C and 3 bar of H_2.

4. Conclusions

Mo supported on activated carbon is active in furfural hydrogenation. The catalytic conversion of the substrate depends on Mo amount: 40%Mo-AC converted 80 % furfural while 10%Mo-AC reached a maximum of 60 % conversion in 6 h of reaction. We addressed this difference to the presence of Mo_4O_{11} orthorhombic phase revealed only in 40%Mo-AC. Ethyl furfuryl ether is formed as the only product in both cases. The addition of Pt to Mo/AC enhances the activity. Pt-AC also showed higher initial activity than Mo-AC. However, they showed a different products distribution, being furfural converted either to ethyl furfuryl ether (80 % selectivity) and furfuryl alcohol (20 % selectivity). Moreover, reaction profiles put in evidence that Pt-containing catalysts tend to deactivate after 6 h. From structural/morphological analyses, we found that Pt nanoparticles supported on Mo-AC have particle size distribution between 1 nm and 3 nm smaller than Pt/AC and more homogeneously dispersed. This could explain the definitely higher catalytic activity of the Pt/Mo system with respect to Pt/AC. The Mo_4O_{11} orthorhombic phase could also play a fundamental role possibly interacting with Pt and promoting hydrogen spill over. Mo-supported on activated carbon is thus a promising material, either as precious metal free-catalyst, or as support, improving Pt nanoparticles distribution and the final catalytic activity in furfural hydrogenation.

Acknowledgements

We thank Mr. Joseba Lizarazu Oses for the contribution in experimental reactions and GC analysis, and Dr. Valentina Colombo for the help with XRD analyses.

References

[1] A. Corma, S. Iborra, A. Velty, Chem. Rev. 107 (2007) 2411–2502.

[2] C. Okkerse, H. van Bekkum, Green Chem. 1 (1999) 107–114.

[3] X. Hu, R.J.M. Westerhof, D. Dong, L. Wu, C.Z. Li, ACS Sustainable Chem. Eng. 2 (2014) 2562−2575.

[4] J.P. Lange, E. Van der Heide, J. Van Buijtenen, R. Price, ChemSusChem 5 (2012), 150−166.

[5] E. I. Gürbüz, J. M. R. Gallo, D. M. Alonso, S. G. Wettstein, W. Y. Lim, J. A. Dumesic, Angew. Chem. Int. Ed. 52 (2013) 1270 –1274.

[6] K. J. Zeitsch, The Chemistry and Technology of Furfural and Its Many By-Products, Vol.13, Elsevier, Amsterdam, The Netherlands, 2000.

[7] J. P. Lange, E. van der Heide, J. van Buij-tenen, R. Price, ChemSusChem 5 (2012) 150–166.

[8] S. De, S. Dutta, B. Saha, Catal. Sci. Technol. 6 (2016) 7364-7385.

[9] G.W. Huber, S. Iborra, A. Corma, Chem. Rev. 106 (2006) 4044-4098.

[10] P. Gallezot, Chem. Soc. Rev. 41 (2012) 1538–1558.

[11] Y. Nakagawa, K. Takada, M. Tamura, K. Tomishige, ACS Catal. 4 (2014) 2718−2726.

[12] V. Vorotnikov, G. Mpourmpakis, D.G. Vlachos, ACS Catal. 2 (2012) 2496−2504.

[13] S.H. Pang, C.A. Schoenbaum, D.K. Schwartz, J.W. Medlin, ACS Catal. 4 (2014) 3123−3131.

[14] S.M. Rogers, C. R. A. Catlow, C. E. Chan-Thaw, A. Chutia, N. Jian, R. E. Palmer, M. Perdjon, A. Thetford, N. Dimitratos, A. Villa, P.P. Wells, ACS Catal. 7 (2017) 2266−2274.

[15] A. Kaufman, J.C. Adams, J. Am. Chem. Soc. 45 (1923) 3029-3044.

[16] J. Kijeński, P. Winiarek, T. Paryjczak, A. Lewicki, A. Mikołajska, Appl. Catal. A: Gen. 233 (2002) 171-182.

[17] P. D. Vaidya, V. V. Mahajani, Ind. Eng. Chem. Res., 42 (2003) 3881–3885.

[18] M. J. Taylor, L. J. Durndell, M. A. Isaacs, C. M.A. Parlett, K. Wilson, A. F. Lee, G. Kyriakou, Appl. Catal. B: Env. 180 (2016) 580-585.

[19] A. Villa, S. Campisi, C. Giordano, K. Otte, L. Prati, ACS Catal. 2(7) (2012) 1377–1380.

[20] M.A. Patel, M.A.S. Baldanza, V.Teixeira da Silva, A.V. Bridgwater, Appl. Catal. A: Gen. 458 (2013) 48-54.

[21] L.A. Sousa, J.L. Zotin, V. Teixeira da Silva, Appl. Catal. A: Gen. 449 (2012) 105-111.

[22] X. Chen, H. Li, H. Luo, M. Qiao, Appl. Catal. A: Gen. 233 (1–2) (2002) 13-20.

[23] a) A. Villa, D. Wang, D. Sheng Su, L. Prati, Catal. Sci. Technol. 5 (2015) 55-68; b) D. M. Alonso, S. G. Wettstein, J. A. Dumesic, Chem. Soc. Rev. 41 (2012) 8075–8098.

[24] a) Y. I. Yermakov, B. N. Kuznetsove, Y. A. Ryndin, J. Catal. 42 (1976) 73; b) T.M. Tri, J.P. Candy, P. Gallezot, J. Massardier, M. Primet, J.C. Vedrine, B.J. Imelik, J. Catal. 79 (1983) 396; c) T.M. Tri, J. Massardier, P. Gallezot, B.J. Imeik, J. Catal. 85 (1984) 244.

[25] G. Leclercq, T. Romero, S. Pietrzyk, J. Grimblot, L. Leclercq, J. Mol. Catal. 25 (1984) 67.

[26] S. Hee Choi, J. Sung Lee, J. Catal. 167 (1997) 364–371.

[27] O. Ioannidou, A. Zabaniotou, Renew. Sust. Energ. Rev. 11 (2007) 1966-2005.

[28] L. Prati, D. Bergna, A. Villa, P. Spontoni, C. L. Bianchi, T. Hu, H. Romar, U. Lassi, Catal. Today 301 (2018) 239-243.

[29] A. Jouve, M. Stucchi, I. Barlocco, C. Evangelisti, F. Somodic, A. Villa, L. Prati, Top. Catal. (2018) 1-11.

[30] S. Brunauer, P.H. Emmett, E. Teller, J. Am. Chem. Soc. 60 (1938) 309-319.

[31] D. Padovan, A. Al-Nayili, C. Hammond, Green Chem. 19 (2017) 2846.

[32] Y. Wang, Q. Cui, Y. Guan, P. Wu, Green Chem. 20 (2018) 2110 -2117.

[33] B. Vanderhaegen, H. Neven, L. Daenen, K. J. Verstrepen, H. Verachtert, G. Derdelinckx, J. Agric. Food Chem. 52 (2004) 1661−1668.

[34] J. Lange, E. van der Heide, J. van Buijtenen, R. Price, ChemSusChem 5 (2012) 150-166.

[35] R. J. Haan, J.P. Lange (Shell), WO-2009/77606, 2009.

[36] X. Chen, H. Li, H. Luo, M. Qiao, Appl. Catal. A: Gen. 233(1–2) (2002) 13-20.

[37] M. C. Abello, M.F. Gomez, O. Ferretti, Appl. Catal. A: Gen. 207(1–2) (2001) 421-431.

[38] M. J.Taylor, L. J.Durndell, M. A.Isaacs, C. M.A. Parlett, K. Wilson, A. F. Lee, G. Kyriakou, Appl. Catal. B: Env. 180 (2016) 580-585.

[39] F. Yang, F. Li, Y. Wang, X. Chen, D. Xia, J. Liu, J. Mol. Catal. A: Chem. 400 (2015) 7–13.

Supporting Information

1. Acidity measurements

Acidity of the support and loaded catalysts was evaluated by NH_3 probe adsorption in flowing dynamic experiments. Samples were crushed in order to obtain particles in the range of 20-45 mesh, dried at 80 °C overnight, and treated at 80 °C under flowing air for 30 minutes to desorb impurities and remove physically adsorbed water. A NH_3/N_2 mixture (1 % mol/mol), with NH_3 concentration of 170 ppm, is fluxed through the sample at 4 NL h^{-1} at 80 °C and entered in a gas cell (path length 2.4 m multiple reflection gas cell) in the beam of a FT-IR spectrophotometer (Bio-Rad with DTGS detector). NH_3 was completely adsorbed. The signal of the NH_3 line at 966 cm^{-1} was recorded as a function of time.

From the evaluation of the time during which NH_3 was not at the starting concentration level and assuming a 1:1 stoichiometry for the NH_3 adsorption on the surface acid site, the amount of acid sites per sample mass (in μequiv·g^{-1}) was evaluated, as follows:

$$\frac{\mu moles_{NH3\ (ads)}}{g_{sample}} = \frac{[NH_3]_{fed} \cdot F \cdot t \cdot P}{RT \cdot m_{sample}} \quad \text{(eq.1)}$$

where $[NH_3]_{fed}$ is the flowing NH_3 concentration (ppm), F is the total flow rate of NH_3/N_2 mixture (NL h^{-1}), t is the time during which NH_3 was completely adsorbed (min), P is the pressure (atm) and m_{sample} is the mass of the sample (g).

Table S1. Results of surface acidity of Mo- and Pt-supported catalysts compared with that of the bare activated carbon from birch.

Catalyst	Sample mass in the test (g)	Time[a] (min)	NH_3 fed (ppm)	Acidity ($\mu moles_{NH3(ads)}/g$)
AC	0.0509	57	178	124.3
Pt/AC	0.0520	59	182	123.5
Mo/AC	0.0566	160	160	498.6
Pt-Mo/AC	0.0659	163	160	469.3

Fig. S1. XPS survey spectra of 40%Mo@AC (A), 1%Pt@AC (B) and 1%Pt/40%Mo@AC (C).

A)

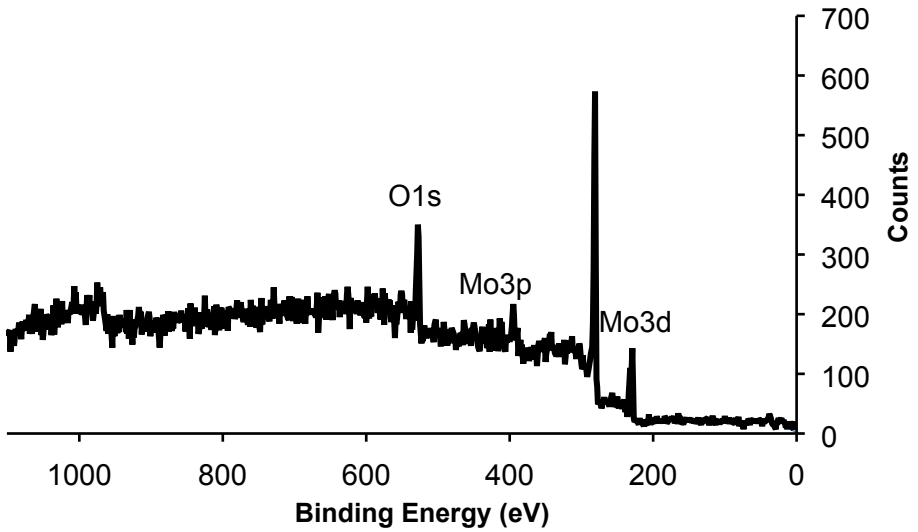

Peak ID	Binding Energy (eV)
Mo 3p	398.4
Mo 3d	232.5
O 1s	531.2
C1s	284.6

B)

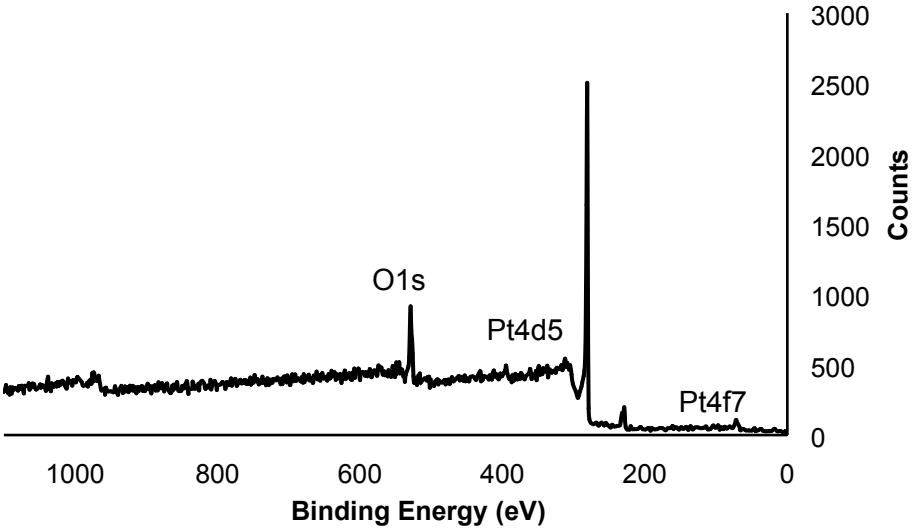

Peak ID	Binding Energy (eV)
Pt $4f_{7/2}$	73.3
C 1s	282.7
Pt $4d_{5/2}$	313.6
O 1s	530.6

C)

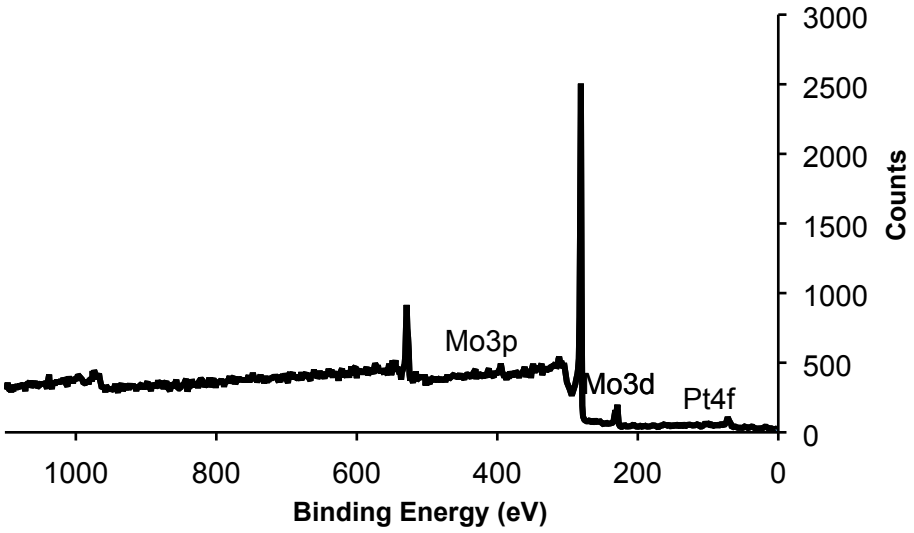

Peak ID	Binding Energy (eV)
Mo 3p	399.0
Mo 3d	232.9
Mo4p	41.3
Pt 4f	74.8
O 1s	531.9
C1s	284.6

Fig. S2. XPS high resolution spectra of C1s (a), O1s (b) and Mo (c) species for 40%Mo@AC.

a

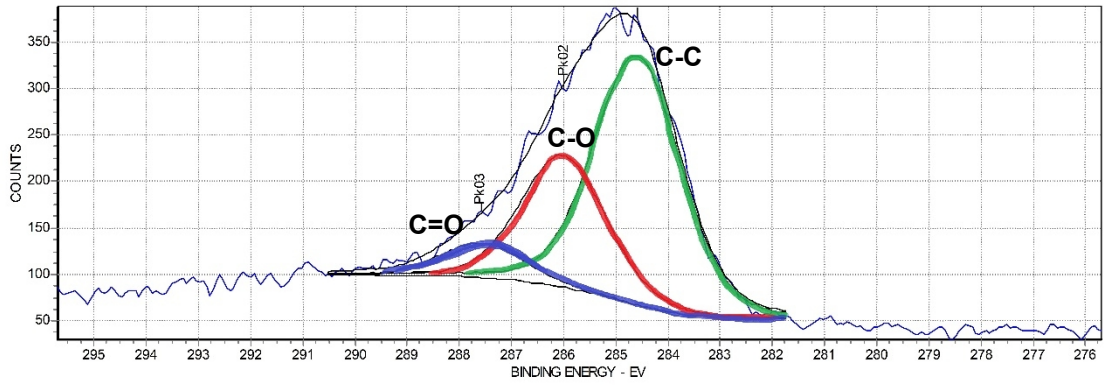

b

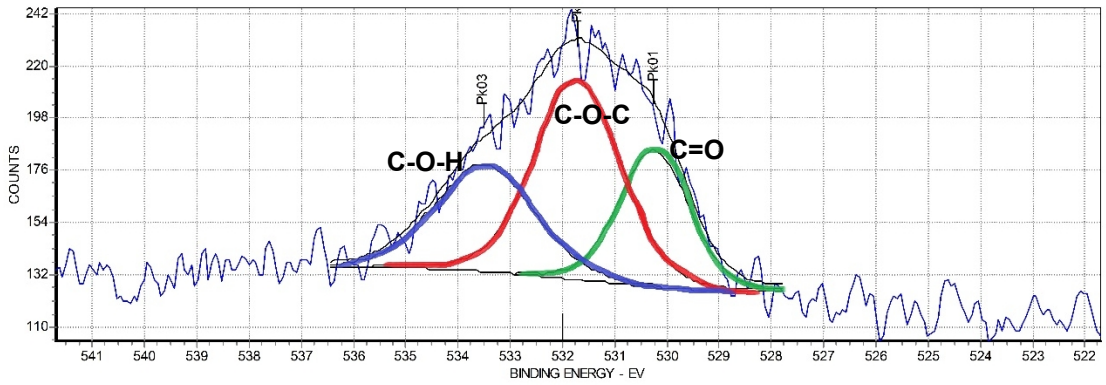

c

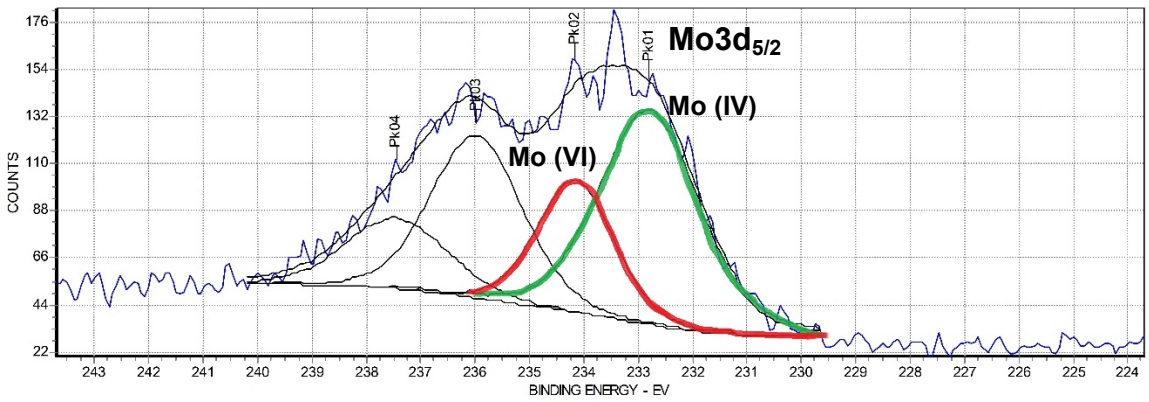

Fig. S3. XPS high resolution spectra of C1s (a), O1s (b) and Pt (c) species for 1%Pt@AC.

a

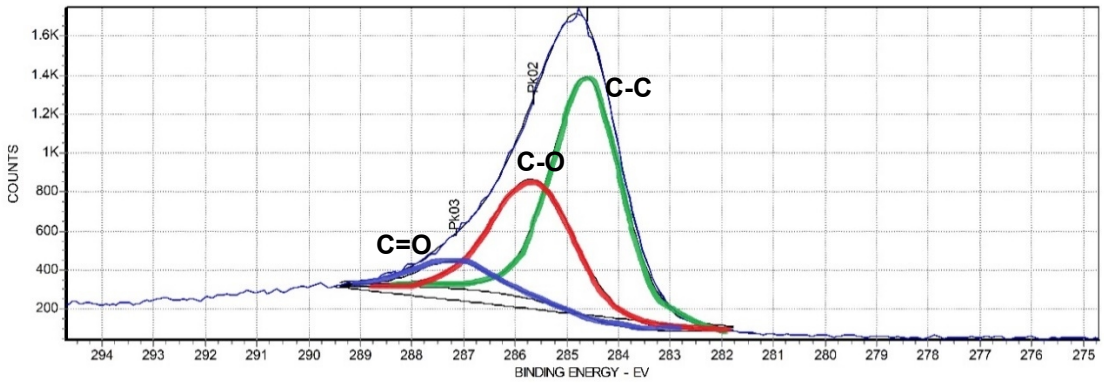

b

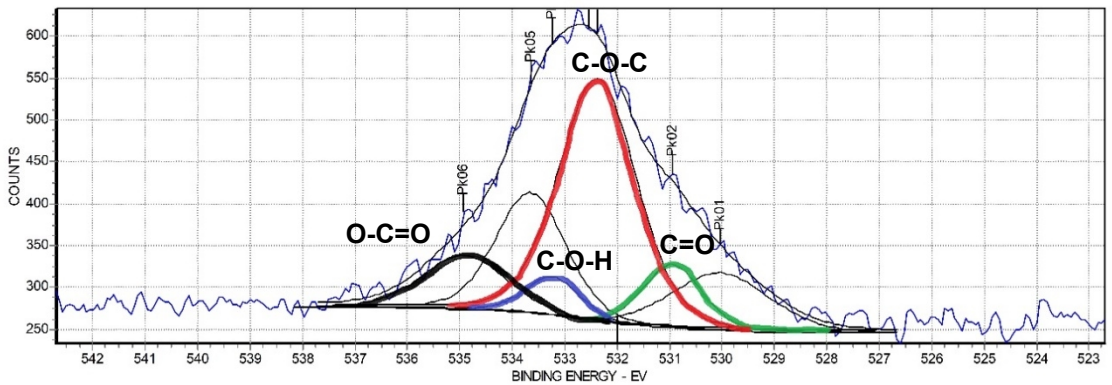

c

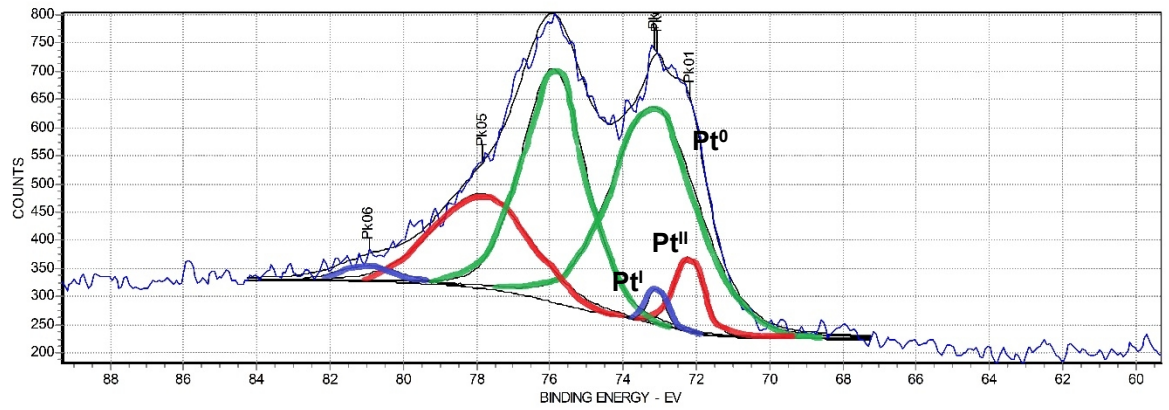

Fig. S4. XPS high resolution spectra of C1s (a), O1s (b), Pt (c) and Mo (d) species for 40%/Mo1%Pt@AC.

a

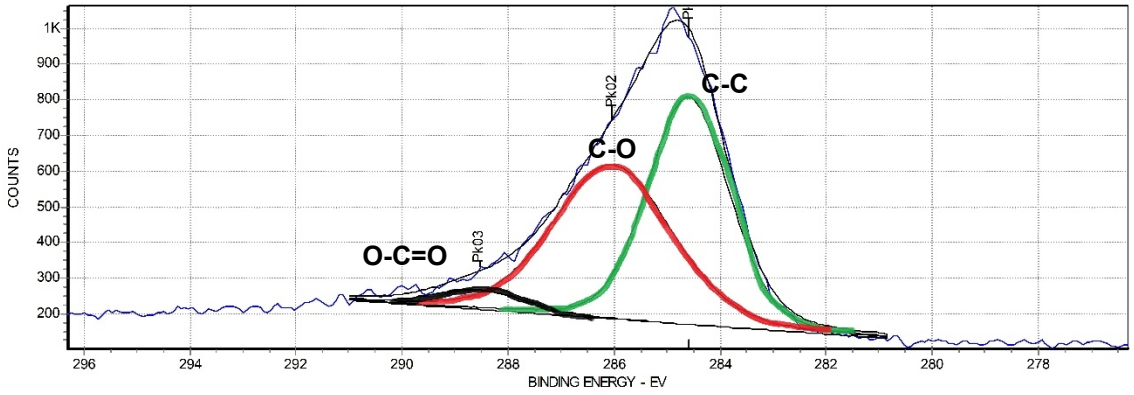

b

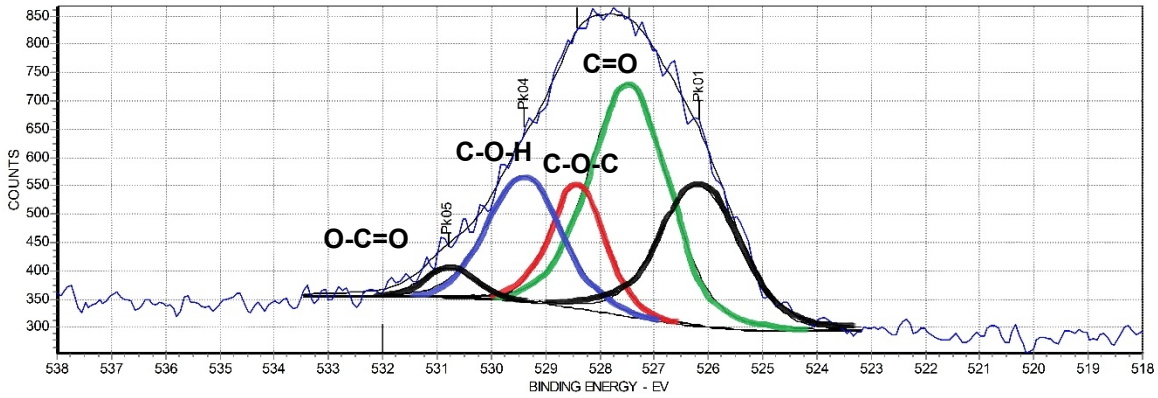

c

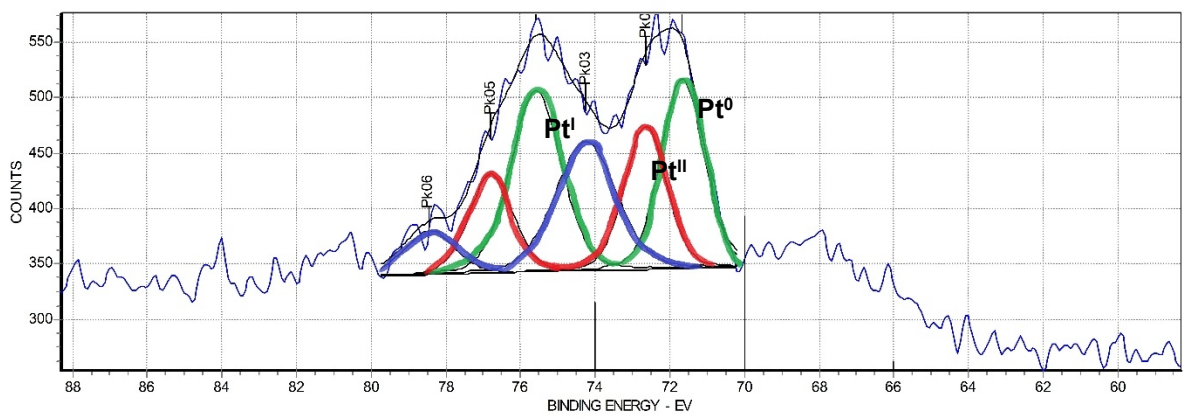
COUNTS
BINDING ENERGY - EV
Pk06
Pk05
Pk03
Pk0
Pt^I
Pt^II
Pt^0

d

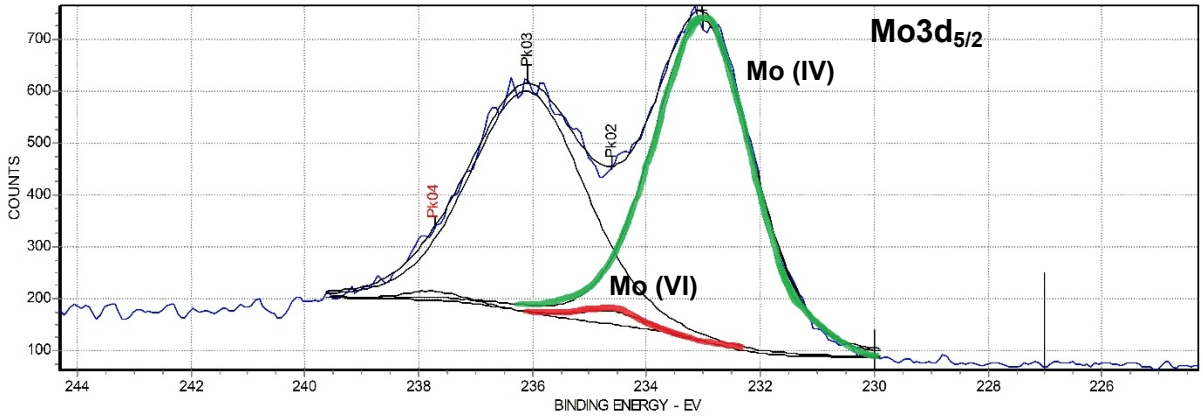
COUNTS
BINDING ENERGY - EV
Pk04
Pk03
Pk02
Mo3d5/2
Mo (IV)
Mo (VI)